Starch modified hyperbranched polyurethane/reduced carbon dot-zinc oxide nanocomposite

Highlight

The present chapter focuses on the preparation, characterization and property evaluation of starch modified hyperbranched polyurethane (HPU) nanocomposite with reduced carbon dot-zinc oxide (RCD-ZnO) nanohybrid. This nanocomposite is studied as a prospective solar energy-assisted heterogeneous photocatalyst for degradation of anionic surfactant contaminants. RCD-ZnO nanohybrid was synthesized by a simple and eco-friendly protocol employing *Colocasia esculenta* leaf extract as a bio-reductant, and the nanocomposite was fabricated with a starch-based HPU by an *in situ* polymerization process. Structural characterizations of the nanohybrid and nanocomposite were performed by various analytical and spectroscopic tools. The fabricated nanocomposite displayed significant enhancement in mechanical and thermal properties. Furthermore, the HPU nanocomposite demonstrated high efficiency as a heterogeneous recyclable photocatalyst for degradation of aqueous surfactant contaminants upon exposure to sunlight. The degradations followed the pseudo-first order kinetics model. Thus, the work holds strong potential for the development of such high performance nanocomposite as an efficient solar energy-assisted heterogeneous recyclable photocatalyst for mass scale applications.

Parts of this work are communicated for publication in

Duarah, R. and Karak, Hyperbranched polyurethane/reduced carbon dot-zinc oxide nanocomposite-mediated solar-assisted photocatalytic degradation of organic contaminant: an approach towards environmental remediation, *Chemical Engineering Journal*, 2018.

5.1. Introduction

As addressed in **Sub-Chapter 4B**, detoxification of industrial contaminants by means of visible light assisted heterogeneous photocatalyst is one of the most significant goals in environmental remediation [1, 2]. Semi-conductors like TiO_2 has been broadly utilized for the degradation of organic pollutants and considered as a standard photocatalytic material [3]. However, TiO_2 restricts its practical applications as it can only respond to UV-light (band gap: 3.2 eV) that comprises barely 4% of entire sunlight [3, 4]. Thus, the development of an effective, economical photocatalyst for degradation of organic pollutants is very essential. In this respect, ZnO proves to be of great potential for water purification and toxic gas detection and thus can be employed as a photocatalyst [5, 6]. However, the large band gap of ZnO is a major limitation for the achievement of high efficiency in its structural system [7]. Thus, the nanohybrid technique was established to improve the performance of ZnO photocatalyst, semiconductor-carbon based nanohybrid, semiconductor-noble metal nanohybrid etc. [8]. Carbon-based nanomaterial(s) (CBN) like reduced graphene oxide (RGO), graphene oxide (GO), carbon nanotube (CNT), etc. are used in the preparation of nanohybrids owing to its adsorption capability, high surface area, super mobility of electron(s) (e^-) and conductivity that benefit the gas sensitive and photocatalytic performances [9, 10]. However, the production of GO, CNT, etc. is extremely tedious and possesses its own downsides with respect to health and ecological problems [11, 12]. In this context, reduced carbon dot (RCD) prospers in preparation of nanohybrids among other CBN like GO, RGO, CNT, etc. As mentioned in the **Sub-Chapter 4A**, the graphitized aromatic structure of RCD supports the homogeneously dispersed nanoparticles and act as a conductive matrix to facilitate superior contact among them. Moreover, during the process of photocatalysis, RCD can efficiently avert aggregation and volume contraction/expansion of nanoparticles and thus, maintain their high active surface area [13]. This, in turn can increase the photocatalytic performance of the RCD based material to some extent. Hence, a nanohybrid comprising of ZnO nanoparticles anchored with electrically conductive graphitized RCD can resourcefully exploit their combined benefits to develop efficient visible light assisted photocatalysts. Also, ZnO nanoparticles can not only enhance the photocatalytic activity due to their plasmonic activity but may also impart antimicrobial property [14]. Although literature cites successful preparation of several graphene-ZnO nanohybrids [15, 16], fabrication of

RCD-ZnO nanohybrid using bio-based resources is not reported till now. Thus, an eco-friendly and simple strategy for the synthesis of RCD-ZnO nanohybrid as an advanced recyclable photocatalyst is reported for degradation of organic pollutants.

As mentioned in the previous chapter, RCD, with its low band gap of (3.1 eV) produces e^--hole (h^+) pairs (e^-/h^+) by absorption of photons (UV) that react with H_2O and O_2 molecules to form hydroxyl ($^{\bullet}OH$) and superoxide active radicals ($^{\bullet}O_2^-$), respectively, which subsequently oxidizes organic contaminant(s) (OC) to H_2O and CO_2. The conducting RCD surface presents highly mobile photo-generated charge carrier which consecutively slows down the recombination of e^-/h^+ pairs. Additionally, the polar surface functional groups in RCD can interact with the OC and facilitate surface adhering which improves the degradation of matter within a short time. In this context, surfactants are one of the most persistent classes of organic pollutants, typically discharged with waste water [17]. Most importantly, degradation of colourless OC like surfactants using sunlight is a daunting challenge as they do not absorb solar light. The bio-elimination and biodegradation of organic surfactants by microorganisms like bacteria are slow and result in foam formation and thus, cause ecological pollution [17, 18]. In this context, dodecyl-benzenesulfonate (DBS) is a common polluting surfactant which is present in synthetic detergents and used widely in industrial and domestic applications [19]. Thus, photocatalysis can be judiciously employed to enhance the degradation of such organic surfactant pollutants.

Thus, an attempt was made to obtain a novel RCD-ZnO nanohybrid using facile and eco-friendly hydrothermal technique. In order to enhance the photocatalytic efficiency of the nanohybrid, different weight percentages of RCD-ZnO was incorporated into the starch modified hyperbranched polyurethane (HPU) to help in easy separation and recycling of the photocatalyst. HPU nanocomposites with self cleaning attributes to remove surfactants from the environment have not been reported till date. Both nanocomposites and bare nanohybrid exhibited potential to be employed as photocatalysts for degradation of DBS and a commercial detergent under normal sunlight which is crucial for their further large scale practical applications.

5.2. Experimental

5.2.1. Materials

Polycaprolactone diol (PCL), toluene diisocyanate (TDI), 1,4-butanediol (BD), starch, ethanol, xylene and N, N-dimethylacetamide of similar specifications and grade were used as described in **Chapter 2** (**Section 2.2.1**) and **Chapter 3** (**Section 3.2.1**). Hyperbranched starch modified polyol (HBSP) was prepared employing the same technique as described in **Chapter 2** (**Section 2.2.3.1**). Zinc chloride ($ZnCl_2$, Sigma Aldrich, Germany) was utilized as received. *Calocasia esculenta* leaf extract was prepared using the same method as described in **Sub-Chapter 4A**. Dodecylbenzenesulfonate (DBS, Merck, India) and a commercial laundry detergent available from the local market in India were employed for the photocatalytic studies. The chief ingredients in the detergent are sodium alkylbenzene sulfonate (anionic surfactant), sodium carbonate (water softener), sodium aluminosilicate (water softener), alcohol ethoxylate (non-ionic surfactant) and sodium perborate monohydrate (mild bleach).

5.2.2. Methods

5.2.2.1. Preparation of RCD-ZnO nanohybrid

In a typical process, 5 mL of ethanolic $ZnCl_2$ solution (0.2 M) was drop wise added to 35 mL of ethanolic NaOH solution (0.5 M), followed by 5 mL of aqueous CD dispersion (solid content 54 mg mL^{-1}, dimension 2.2-5.2 nm) under vigorous stirring. The contents were further subjected to ultrasonication for 20 min for complete homogenization of the reactants. Thereafter, 10 mL of *C. esculenta* aqueous leaf extract with a few drops of $FeCl_3$ (0.01 M) was added to mixture and the mixture was refluxed for 2 h at 80 °C. Subsequently, the solution was cooled to room temperature to obtain a light brown coloured precipitate of RCD-$Zn(OH)_2$. The precipitate was collected by centrifugation at 10,000 rpm for 10 min and washed with deionized water several times to remove the unreacted contents. Ultimately, the RCD-$Zn(OH)_2$ was vaccum dried at 60 °C overnight to obtain RCD-ZnO nanohybrid.

5.2.2.2. Fabrication of HPU nanocomposites

BD (0.36 g, 0.004 mol) and PCL (6 g, 0.002 mol) were taken in a three necked round bottom flask, equipped with a mechanical stirrer and a nitrogen gas inlet. Subsequently, at room temperature, TDI (0.007 mol, 1.22 g) was added slowly into the mixture and stirred at (70 ± 2) °C for 3 h (maintaining -NCO/-OH ratio = 1). After the completion of the reaction, a viscous mass was obtained as the pre-polymer. Next, in the second step, HBSP (1.4 g, 0.01 mol, branch generating moiety) was added to the pre-polymer along with the remaining amount of TDI (0.35 g, 0.002 mol) (maintaining -NCO/-OH = 1). Steadily the temperature was raised to (80 ± 2) °C and stirred for 2 h, continuously. Afterwards the reaction was cooled down to room temperature. RCD-ZnO nanohybrid dispersion in THF (0.5, 1 and 2 wt% with respect to HPU) was added to the reaction mixture and the temperature was steadily raised to (80 ± 2) °C. The reaction was run for 2 h until its completion. Similarly, three separate polymerization reactions were performed to obtain HPU/RCD-ZnO (HPU/RZN) nanocomposites with 0.5, 1 and 2 wt% of RCD-ZnO, as HPU/RZN0.5, HPU/RZN1 and HPU/RZN2, respectively. Moreover, HPU without nanohybrid was also prepared for comparison.

5.2.2.3. Photocatalytic activity

Separate organic surfactant solutions containing DBS and a commercial detergent were used for the determination of photocatalytic degradation activity of HPU nanocomposites. In a typical procedure, small pieces of HPU/RZN2 film (0.5 g) were taken in two separate flasks containing 100 mL aqueous solution of DBS (50 ppm) and a commercial detergent (50 ppm). The solutions were stirred under normal solar light of 60000-80000 lux at room temperature. The changes in concentrations of DBS and the commercial surfactant were monitored by determining UV absorbance intensity at wavelengths of 221 nm under specified time intervals. The activity of the catalyst was calculated from the rate of change of concentration of the surfactant. The same experiment was also conducted using exact amount of the nanohybrid for comparison purposes. The amount of the degraded contaminants was obtained by using the following equation.

$$\text{Degradation (\%)} = [(C_0-C)/C_0 \times 100] \quad \textbf{(Eq. 5.1)}$$

where C_0 = initial concentration and C = concentration after photocatalytic degradation of the pollutant.

5.2.3. Characterization

The instrumentation and characterization techniques for spectroscopic (Fourier-Transform Infrared Spectroscopy (FTIR), X-ray Diffraction (XRD), Ultraviolet–visible (UV-visible) and Raman), microscopic [High-Resolution Transmission Electron Microscopy (HRTEM)], thermal analyses [Thermogravimetric Analysis (TGA) and Differential Scanning Calorimetric (DSC)] and mechanical testing [Universal testing machine (UTM) and impact resistance] were same as mentioned in **Chapter 2** (**Section 2.2.2**) and **Sub-Chapter 4A** (**Section 4A.2.2.3**).

5.3. Results and discussion

5.3.1. Preparation of RCD-ZnO nanohybrid

RCD-ZnO nanohybrid was prepared by a facile solution co-precipitation technique involving *in situ* reduction of CD and Zn precursor (**Scheme 5.1**).

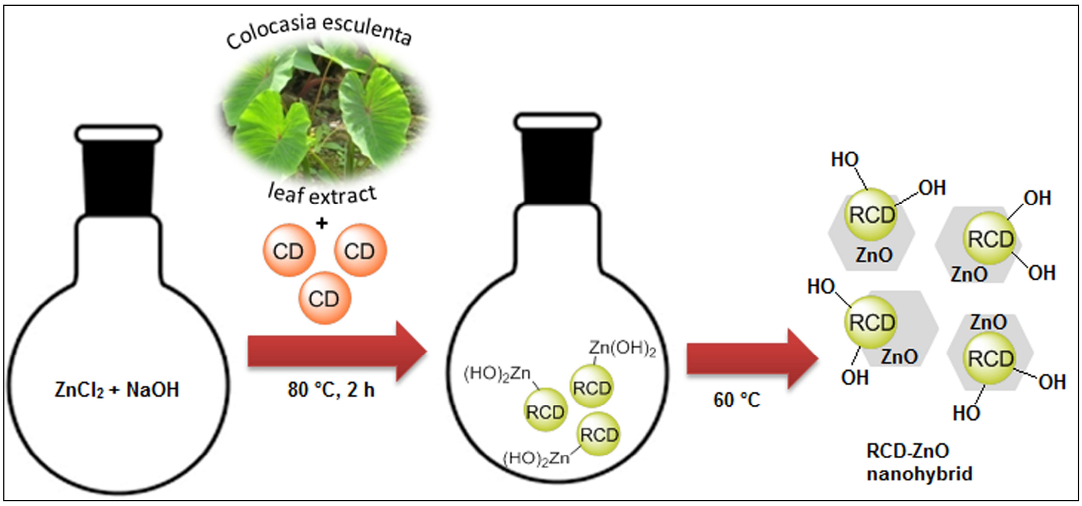

Scheme 5.1 Synthesis of RCD-ZnO nanohybrid.

Initially, Zn precursor and carbon dot (CD) were mixed together in an alkaline medium, forming a Zn^{2+}-CD complex. As mentioned in **Chapter 3** (**Section 3.1**), the CD surfaces are supplemented with various polar functional groups like carboxylic, hydroxyl, epoxy groups, etc. [20, 21]. These peripheral surface polar groups facilitated the complexation of Zn^{2+} ions with CD. It is well known that CD can be further converted to their reduced state, improving certain properties along the way as mentioned in **Sub-Chapter 4B**. Reduction of CD results in decrease of peripheral oxygeneous surface functional groups and generation of near-graphitic core structure, which augments photocatalytic activity. Also, plant phytochemicals act as very good bio-reducing agents, owing to their high polyphenol content [11, 12]. In this route, the reduction of CD was driven by polyphenolic groups present in the *C. esculenta* phytoextract. This polyphenolic reduction process was further augmented by presence of Fe^{3+} ion, forming an effective Fe^{3+}-polyphenol reducing complex [11-13]. Subsequently, Zn^{2+} ions in presence of alkaline medium formed $Zn(OH)_2$, which combined with simultaneously *in situ* RCD, resulting in the formation of RCD-$Zn(OH)_2$. Ultimately, RCD-$Zn(OH)_2$ underwent dehydration, where $Zn(OH)_2$ phase converted to ZnO, generating RCD-ZnO nanohybrid [22].

5.3.2. Characterization of RCD-ZnO nanohybrid

The FTIR spectrum of the nanohybrid revealed changes in functional groups of CD pertaining to the formation RCD-ZnO (**Figure 5.1**).

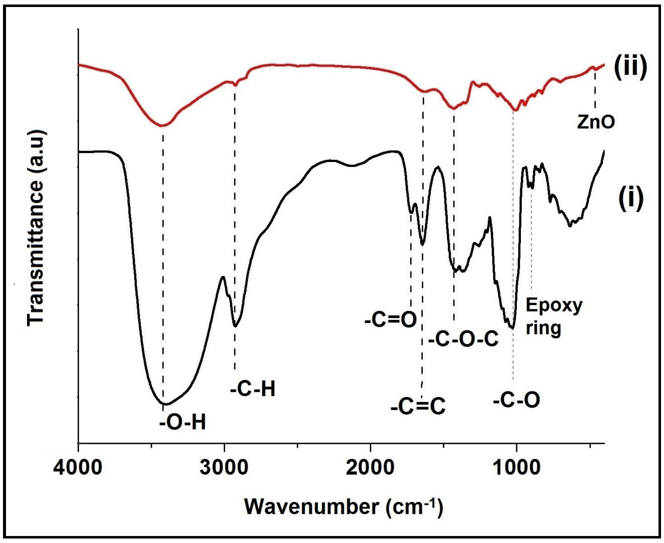

Figure 5.1. FTIR spectra of (i) CD and (ii) RCD-ZnO.

FTIR bands of the nanohybrid were observed at 3404 cm^{-1} (-O-H stretching), 1735 cm^{-1} (-C=O stretching), 1263 cm^{-1} (C-O stretching) to reveal the presence of hydroxyl, carbonyl and carboxylic groups in CD, respectively. Most of the oxygeneous groups present in CD are diminished or completely absent in the spectrum of RCD-ZnO. There was a decrease in the relative intensity of the broad band for the hydroxyl group (at 3404 cm^{-1}), whereas the sharp band of epoxy group (918 cm^{-1}) diminished due to the efficient reduction of CD [20, 21]. The XRD pattern of the nanohybrid clearly confirmed the presence of ZnO in the system (**Figure 5.2**). The nanohybrid displayed all the diffraction peaks consequent to (100), (002), (101), (102), (110), (103) and (112) Braggs lattices of the ZnO hexagonal structure (JCPDS 79-2205) [23]. The broad peak of RCD appeared at 23.2° corresponding to (002) plane of graphitic carbons. This suggested that RCD and ZnO are embedded together and held by good interfacial interactions. The Raman spectrum of RCD-ZnO (**Figure 5.3**) with the characteristic D band (1361 cm^{-1}), G band (1593 cm^{-1}) and 2D band (2914 cm^{-1}) clearly specified an increase in the I_D/I_G ratio on transformation of CD (1.16) to RCD-ZnO nanohybrid (1.64). This is ascribed to the fact that upon reduction of CD, there is an increase in number of *sp*^{2} domains and at the same time decrease in their average sizes. This outcome reflects the elimination of various oxygeneous groups present in RCD, leading to the restoration of aromatic conjugation of their domains, but further generating a disordered structure due to the intensive interactions between ZnO species and RCD.

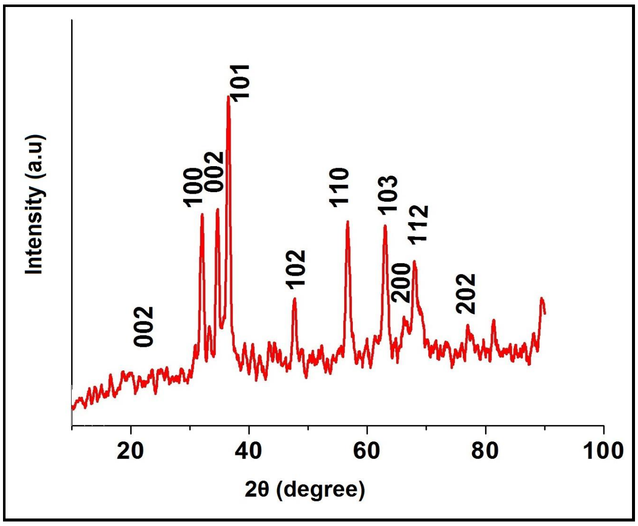

Figure 5.2. XRD pattern of RCD-ZnO.

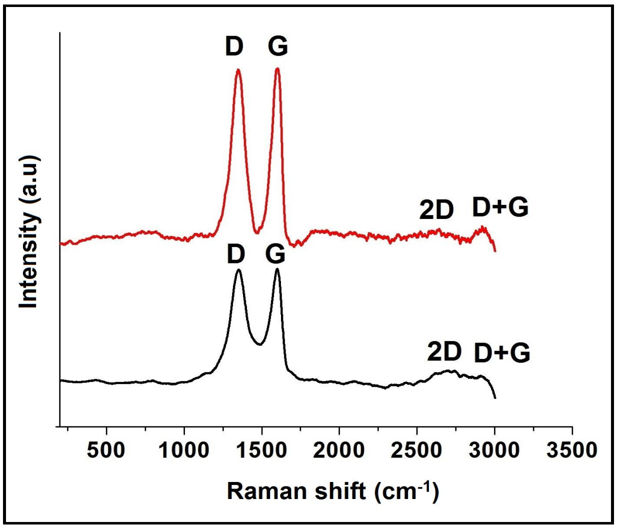

Figure 5.3. Raman spectra of (i) CD and (ii) RCD-ZnO.

These interactions create new graphitic domains that are smaller in size to the ones present in CD, prior reduction, but more in number which generates a disordered nanohybrid structure that leads to decrease in domain size of the restored aromatic conjugation. The formation of hexagonal ZnO nanoparticles embedded on RCD can be confirmed from HRTEM images of RCD-ZnO nanohybrid (**Figure 5.4**). Good interactive forces hold together RCD and ZnO which assist in mutually stabilizing one another. The diameter of RCD and ZnO are found in the range of 3-5 nm and 10-12 nm, respectively.

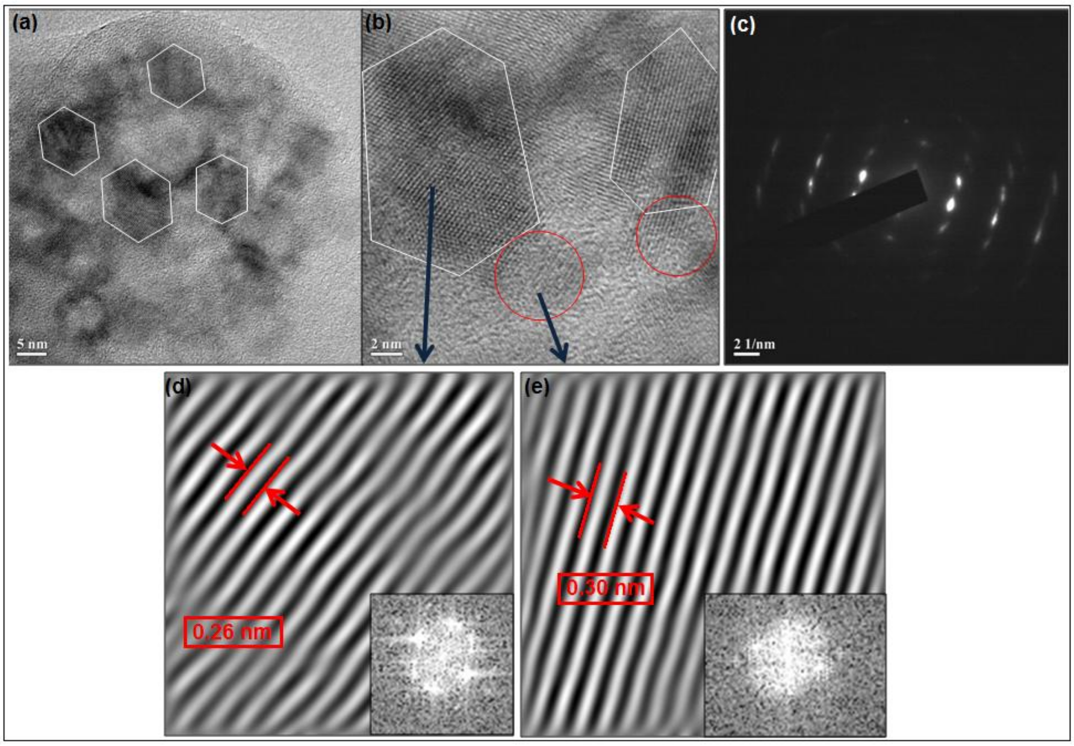

Figure 5.4. TEM images of RCD (red lines) and ZnO (white lines) at magnification **(a)** 5 nm, **(b)** 3 nm; **(c)** SAED pattern of RCD-ZnO nanohybrid; IIFT images with lattice fringes of **(d)** ZnO (inset FFT image) and **(e)** RCD (inset FFT image) in the nanohybrid.

The average nanomaterial size of ZnO has also been calculated from the XRD pattern of RCD-ZnO, using the Scherrer equation, by taking three most intense peaks of ZnO (36.4°, 34.64° and 32°).

Crystallite size $Dp = K\lambda/(B \cos\theta)$………………………. **(Eq. 5.2)**

Where, Dp = average nanomaterial size, K = Scherrer constant, λ = X-ray wavelength, B = FWHM (full width at half maximum) of XRD peak, θ = XRD peak position, one half of 2θ. The average size of the ZnO nanomaterial was calculated to be 11.55 nm which is well agreed with the values 10-12 nm calculated from TEM images. The crystal lattice fringes of RCD within the RCD-ZnO nanohybrid with a *d*-spacing of 0.32 nm corresponds to (002) plane of graphitic RCD as revealed by IFFT image. On the other hand, the distinct lattice fringe of 0.26 nm in the nanohybrid corresponds to (002) plane of hexagonal ZnO phase. This indicates that the preferential growth of ZnO is along [001] direction in the nanohybrid [24]. Moreover, the SAED pattern of the nanohybrid suggests a crystalline and a well-ordered structure of the nanohybrid. The actual content of the Zn, O and C was determined by EDX study at two different points of the RCD-ZnO nanohybrid (**Figure 5.5**). From the TEM analysis, the point at ZnO nanoparticle is analyzed where the weight percentages of Zn, C and O are found to be 41.4%, 22.2% and 36.28%, respectively (**Figure 5.5a**). At this point, the C/O ratio is found to be 0.61 which confirms the presence of ZnO. Similarly, the point at RCD is analyzed where the weight percentages of Zn, O and C are found to be 11.8%, 5.82% and 82.34%, respectively (**Figure 5.5b**). The C/O ratio at this point is 14.1 which confirms the presence of RCD which agrees with the previously determined value of RCD.

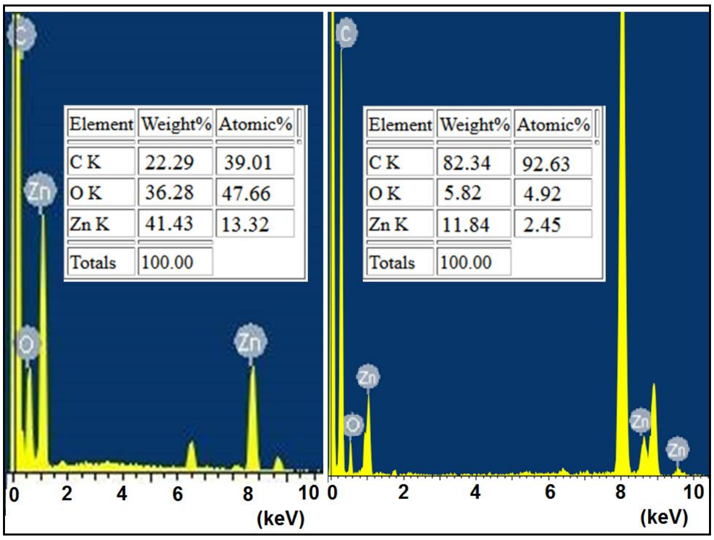

Element	Weight%	Atomic%
C K	22.29	39.01
O K	36.28	47.66
Zn K	41.43	13.32
Totals	100.00	

Element	Weight%	Atomic%
C K	82.34	92.63
O K	5.82	4.92
Zn K	11.84	2.45
Totals	100.00	

Figure 5.5. EDX maps of (a) ZnO phase and (b) RCD phase in RCD-ZnO nanohybrid

5.3.3. Fabrication of HPU nanocomposites

An *in situ* polymerization method was employed to fabricate the HPU/RZN nanocomposites (**Scheme 5.2**). The fundamental aspects for the successful fabrication of the nanocomposite are concentration of the reactants, nature and amount of nanohybrid, temperature, reaction time and rate of addition of the branching moiety as mentioned in **Chapter 2** (**Section 2.3.3**).

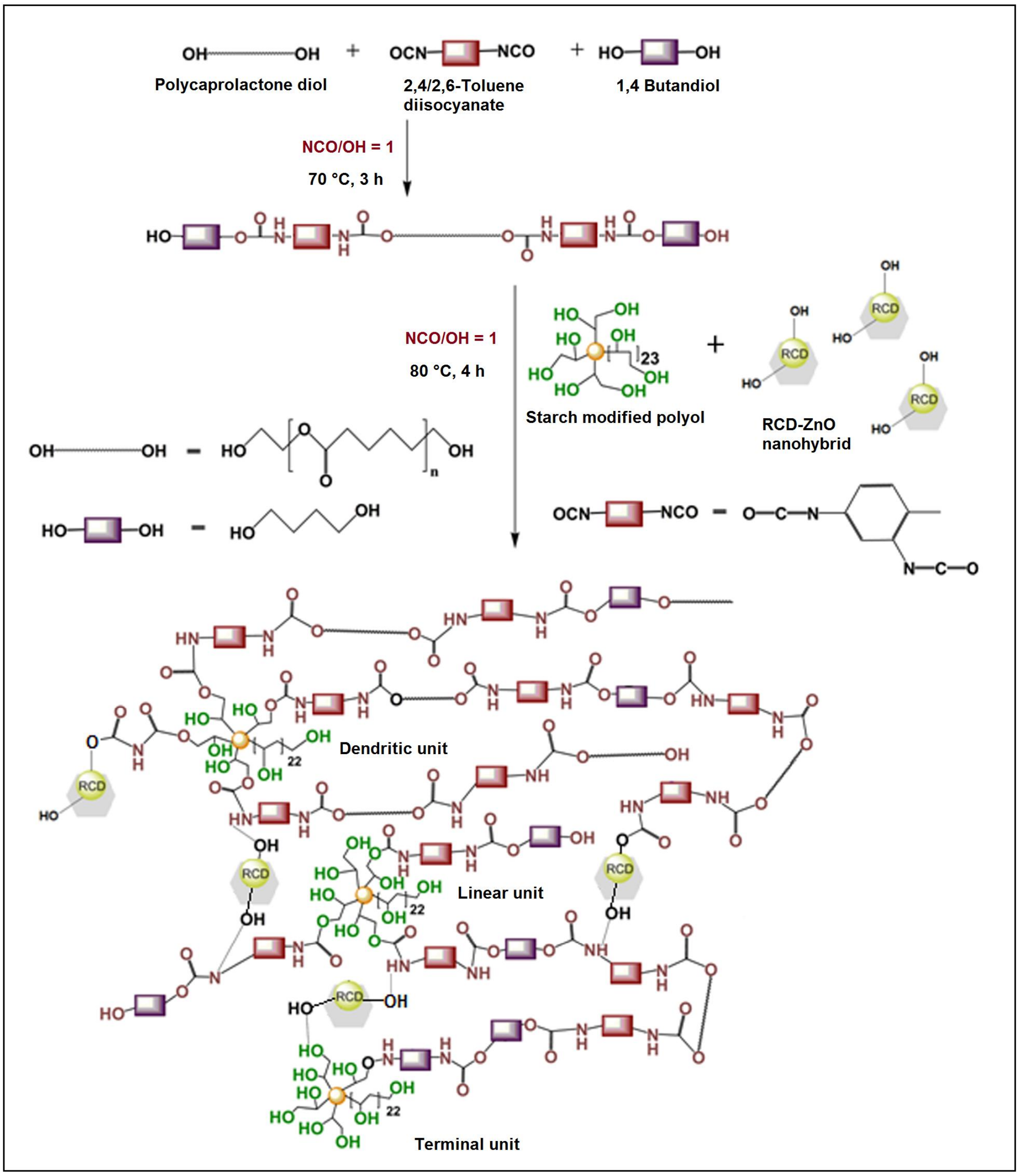

Scheme 5.2. Synthesis of HPU/RZN nanocomposite.

Consequently, in the second step, branching unit was taken in a dilute xylene solution (15-20)% and added drop-wise at room temperature. Also, the RCD-ZnO nanohybrid was slowly incorporated in the second step to attain strong interfacial interactions with the HPU matrix. Strong interfacial interactions result in better stabilization of nanohybrid within the matrix.

5.3.4. Characterization of HPU nanocomposites

The disappearance of the free –NCO group band at 2270 cm^{-1} in the FTIR spectra of HPU nanocomposites (**Figure 5.6**) confirmed the completion of the reaction [13].

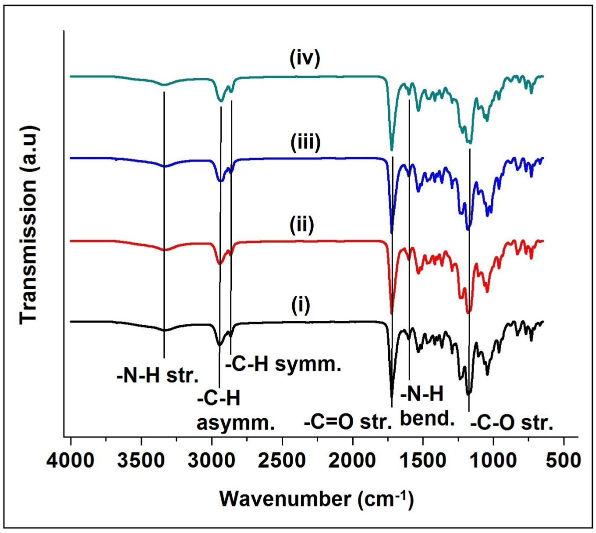

Figure 5.6. FTIR spectra of (i) HPU, (ii) HPU/RZN0.5, (iii) HPU/RZN1 and (iv) HPU/RZN2.

Further, the FTIR study of the HPU nanocomposites displayed the characteristic bands of pristine HPU. The vibration bands near 1680 cm^{-1} are attributed to C=O stretching vibration (due to amide I and ester linkage) [25]. Additionally, N–H stretching and N–H bending vibrations were observed at 3433 cm^{-1} and 1598 cm^{-1}, respectively. At 2954 cm^{-1} (asymmetric C-H vibration), 2867 cm^{-1} (symmetric C-H vibration), 1062-1093 cm^{-1} (N-H deformation vibration), 1177-1225 cm^{-1} (C-O stretching vibration) and a few characteristic bands for urethane linkage were observed. The increased amount of nanohybrid brought about a shift in the C=O band from 1695 cm^{-1} to 1683 cm^{-1} in the nanocomposites.

This specifies the presence of interactions among the polymer chains and the nanohybrid that increase with an increase in the nanohybrid content [25, 26]. Two distinct peaks at 2θ = 21.24° (*d*-spacing = 0.41 nm) and 23.51° (*d*-spacing = 0.375 nm) were observed in the XRD patterns of HPU nanocomposites (**Figure 5.7**), attributed to (110) and (200) crystal planes of the PCL moiety present in HPU matrix [13, 26]. The PCL peaks shifted slightly towards a higher angle upon addition of the nanohybrid which may be attributed to the formation of a dense structure of HPU nanocomposite.

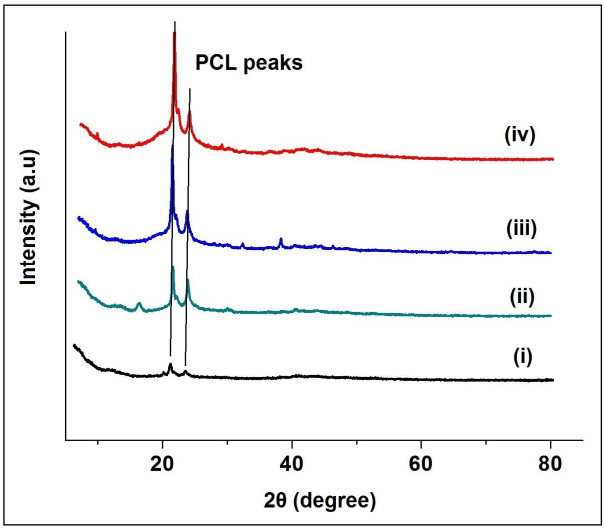

Figure 5.7. XRD maps of (i) HPU, (ii) HPU/RZN0.5, (iii) HPU/RZN1 and (iv) HPU/RZN2.

This further specifies that the nanohybrid acts as a nucleating agent which results in higher crystallinity of the nanocomposites on increasing the nanohybrid content [25, 26]. However, due to the presence of a very small amount of RCD-ZnO in the nanocomposite (0.5-2.0 wt% of total amount of HPU), no peak for RCD-ZnO was observed in the XRD patterns of the nanocomposites. The homogeneous distribution of RCD-ZnO nanohybrid within the HPU/RZN matrix was unveiled from bulk morphology investigation by TEM analysis (**Figure 5.8**).

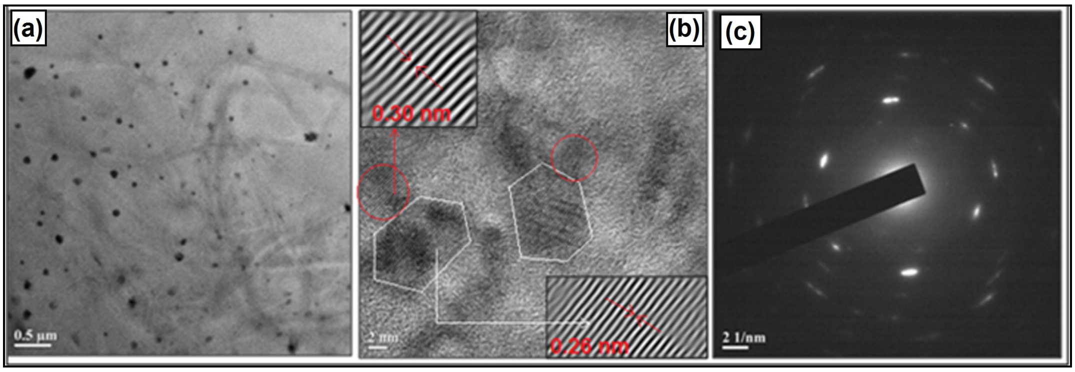

Figure 5.8. TEM image of HPU/RZN2 at magnification (c) 0.5 µm, (d) 2nm with lattice fringes of RCD (red lines) and ZnO (white lines) of nanohybrid at inset; and (e) SAED pattern of RCD-ZnO nanohybrid in the HPU matrix.

5.3.5. Mechanical properties

The mechanical performance of the nanocomposites provided notable insights into their quality and applicability. The results demonstrated significant enhancements in most of the mechanical properties of the nanocomposites (**Table 5.1**).

Table 5.1 Mechanical properties of HPU and its nanocomposites

Property	**HPU**	**HPU/RZN0.5**	**HPU/RZN1**	**HPU/RZN2**
Tensile strength (MPa)	17.6 ± 1.2	24.97 ± 1.2	30.3 ± 1.4	33.6 ± 1.3
Elongation at break (%)	1158 ± 15.2	1192.2 ± 14.2	1462.3 ± 15.5	1614.5 ± 12.3
Toughness[a] (MJ m^{-3})	136.73 ± 10.3	236.6 ± 8.3	378.6 ± 7.3	482.3 ± 8.4
Scratch hardness (kg)	6.5 ± 2	>10	>10	>10
Impact strength[b] (kJ m^{-1})	>19.02	>19.02	>19.02	>19.02

[a] *Calculated by integrating the area under stress-strain curves.*

[b] *Maximum limit of the instrument.*

Moreover, all the nanocomposites showed nanohybrid loading-dependent enhancement of mechanical properties, even at very low loading percentage 0.5-2.0 wt%. Tensile strength of the nanocomposites magnified up to almost 194%

(maximum), displaying a linear increasing trend with percent nanohybrid loading. Elongation at break of the nanocomposites displayed a similar increase up to almost 139% (maximum) in tandem with increasing nanohybrid loading. Simultaneously, the measurement of toughness from stress-strain profiles of the nanocomposites revealed hugely improved values up to almost 354% (maximum) on increasing nanohybrid loading (**Figure 5.9a**).

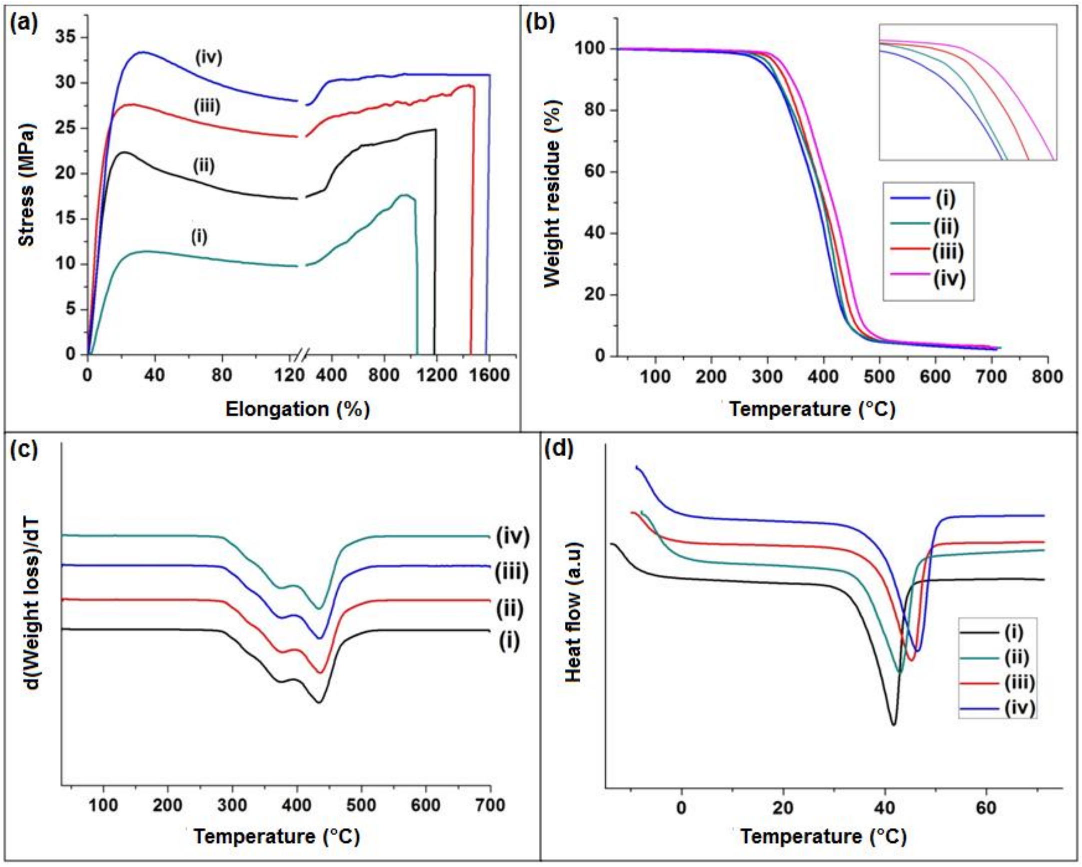

Figure 5.9. (a) Stress-strain profiles, **(b)** TGA thermograms, **(c)** DTG curves and **(d)** DSC curves of (i) HPU, (ii) HPU/RZN0.5, (iii) HPU/RZN1 and (iv) HPU/RZN2.

Along the same lines, the nanocomposites demonstrated high values of impact strength and scratch hardness, although the precise values could not be calculated as they surpassed the limiting values of the equipments used. It is well known that CBN like carbon nanotube, graphene, CD, etc. can effectively improve material properties of polymers [26]. In this context, the enhanced mechanical performance of HPU nanocomposites is mainly attributed to uniform dispersion and good reinforcing ability of RCD. The incorporation of carbonized nanohybrid into the HPU matrix offered substantial reinforcement of the matrix, by means of physico-chemical interactions [13, 26]. This reinforcement provided the right amount of rigidity and flexibility to the HPU matrix resulting in overall high mechanical performance.

5.3.6. Thermal properties

The thermal stability of HPU/RZN nanocomposites was ascertained by conducting thermogravimetric study. The thermograms of the nanocomposites (**Figure 5.9b**) revealed high thermal degradation temperatures beyond 300 °C. In fact, all the nanocomposites demonstrated higher thermal stability in comparison to the pristine HPU. This superior thermal stability is mainly attributed to the reinforcement of the HPU matrix by RCD-ZnO nanohybrid. The RCD-ZnO nanohybrid populated in the free volume of the HPU matrix and interacted with the polymer matrix by various physico-chemical interactions, thereby strengthening the matrix. This reinforcement of the matrix led to the restricted thermal motions of the polymeric chains and imparted resistance to degradation/pyrolysis of the matrix, thus making the process more energy consuming [13]. This thermal stability was further evident from the char residue of the nanocomposites left behind. Incorporation of CBN and metallic particles are known to enhance thermal stability, by absorbing the thermal radiation and hindering the degradation of the polymer matrix [26]. The DTG curves of the nanocomposites (**Figure 5.9c**) divulged a two-step thermal degradation pattern similar to the pristine HPU, accredited to the inherent soft and hard segments in HPU matrix [13, 26]. Notably, some overlapping of the curves was also observed in their corresponding thermogravimetric thermograms which can be attributed to a similar decomposition mechanism of segments of the HPU matrix. This observation suggested that the loading and nature of the nanomaterial did not significantly control the degradation of the fabricated nanocomposites [13, 25]. Moreover, the HPU nanocomposites displayed loading-dependent enhancement of thermal degradation temperatures, even at very low loading percentages. Enhancement of peak degradation temperatures and char residue percentages of nanocomposites were observed on gradually increasing the loading of the nanohybrid (**Table 5.2**).

Table 5.2. Thermal properties of HPU and its nanocomposites

Property	HPU	HPU/RZN0.5	HPU/RZN1	HPU/RZN2
Peak temperature (1st stage degradation) (°C)	371	384	390	396
Peak temperature (2nd stage degradation) (°C)	436	446	450	456
Weight residue (%)	3.4	3.5	3.5	3.7
Melting temperature (T_m, °C)	40.2	45.6	48.6	54.8
Melting enthalpy (ΔH_m, J g^{-1})	43.4	48.5	52.3	58.3

This indicated excellent reinforcing ability of the RCD-ZnO nanohybrid, as more content of nanohybrid incorporated in the HPU matrix resulted in a compact and strong nanocomposite system, less prone to thermal decomposition.

Again, the melting enthalpy (ΔH_m), melting temperature (T_m) and crystallinity of the nanocomposite were explored by conducting DSC analyses (**Figure 5.9d**). The T_m of the soft segment shifted to higher temperature with increase in the nanohybrid content (**Table 5.2**). The T_m of the nanocomposites improved as the polymeric molecular chains were arranged appropriately due to presence of nanohybrid. ΔH_m values can also determine the amount of crystallinity in the nanocomposites (**Table 5.2**). The enhancement of crystallinity of semi crystalline polymer with the integration of different nanomaterials has been cited in previous reports. Thus, the uniformly distributed nanohybrid acts as a nucleating agent, arranging the soft segment in a definite direction by boosting the crystallization process [25, 26].

5.3.7. Optical properties

The formation of RCD-ZnO nanohybrid was monitored by taking a UV visible spectrum of the initial mixture of CD, *C. esculenta* leaf extract and $ZnCl_2$, which showed a broad peak at 400 nm corresponding to Zn^{2+} and a peak at 275 nm attributed to CD (**Figure 5.10a**).

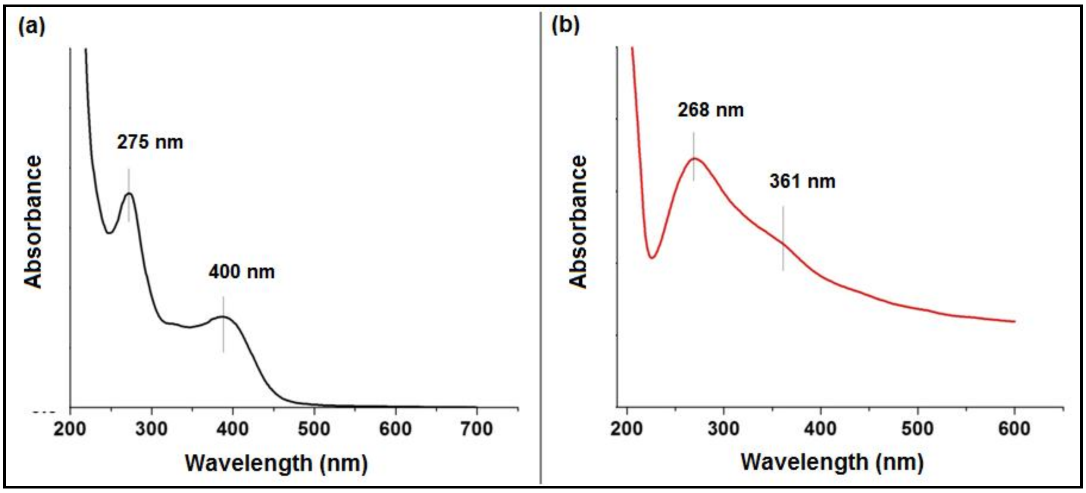

Figure 5.10. UV visible spectra of **(a)** initial mixture of RCD-ZnO precursor and **(b)** RCD-ZnO

However, UV visible spectrum of the nanohybrid [**Figure 5.10b**] shows that the peak at 400 nm exhibited a blue shift to 361 nm due to surface plasmon resonance (SPR) effect of bulk ZnO nanoparticles [27]. The spectrum of the nanohybrid also displayed a blue shift of the peak at 275 nm to 268 nm due to the restoration of electronic conjugation on formation of multilayered graphitic RCD structure (**Figure 5.10b**) [14]. Moreover, the UV visible spectrum of nanohybrid exhibited a broad absorption band over a wide range of wavelengths from 200 nm to 800 nm, indicating effective photo-absorption that would be useful for its photocatalytic activity under visible light [27, 28]. The UV-visible spectra can also be utilized to determine the optical band gap of RCD-ZnO and RCD using the equation below.

$$\alpha = C(h\nu - E_{bulk})^{1/2}/h\nu \ldots\ldots\ldots\ldots\ldots\ldots\ldots\ldots\ldots\ldots \textbf{(Eq. 5.3)}$$

where h = plank’s constant, α = absorption coefficient, ν = frequency, E_{bulk} = bulk ‘band gap’ and C = constant. By extrapolating a linear regression to $(\alpha h\nu)^2 = 0$ in the plot of $h\nu$ versus $(\alpha h\nu)$, the band gaps can be calculated. The optical band gap of RCD-ZnO (2.12 eV) was found to be considerably lowered as compared to bare RCD (3.18 eV) and bare ZnO (3.3 eV) **(Figure 5.11)**. This lowering of band gap is attributed to overlapping of energy levels of RCD and ZnO, on formation of nanohybrid. The overlapping of energy levels resulted in increasing of the valence band maximum and decreasing of the conductance band minimum, thereby lowering the overall band gap of the nanohybrid.

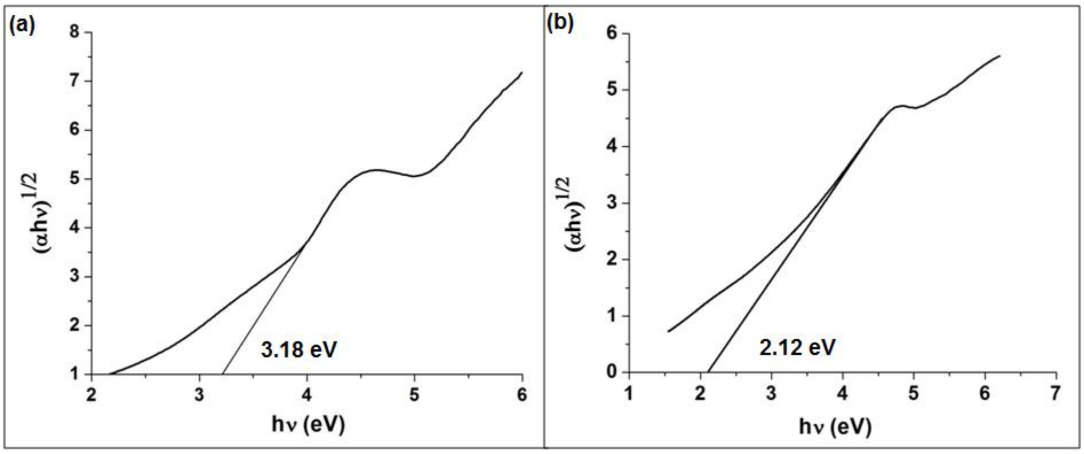

Figure 5.11. $(\alpha h\nu)^{1/2}$ vs hν plots for **(a)** RCD, and **(b)** RCD-ZnO.

Moreover, the optimum band gap of HPU/RZN2 was determined to be 2.08 eV, which is comparable to that of bare nanohybrid (**Figure 5.12**). The slight decrease in the band gap of the nanocomposite can be attributed to the physico-chemical interactions between the nanohybrid and the HPU matrix. These physico-chemical interactions enabled further efficient charge carrying ability of the photo-generated e^-/h^+ pairs, thus leading to enhanced photocatalytic activity under sunlight. The photoluminescence (PL) study of RCD-ZnO provides insight into its optical activity and transfer behavior of the photo-generated charge carriers.

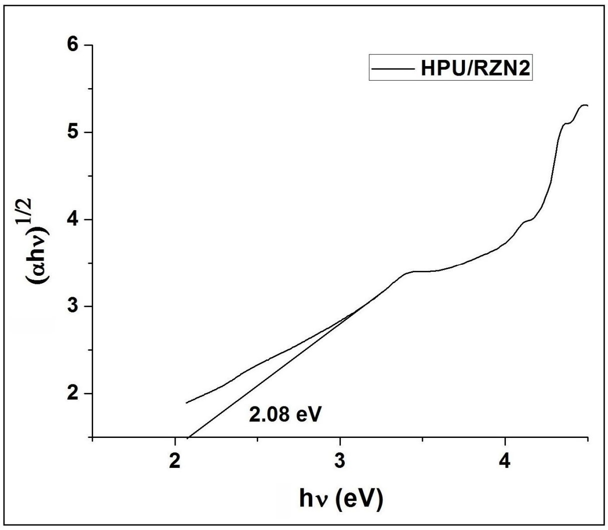

Figure 5.12. $(\alpha h\nu)^{1/2}$ vs hν plot for HPU/RZN2

The PL emission spectra of RCD-ZnO (1 mg mL^{-1}) revealed a broad maximum emission peak at 698 nm on excitation at 340 nm, which was found to be comparable with the maximum emission peak of RCD (1 mg mL^{-1}) at 857 nm under the same excitation wavelength (**Figure 5.13a**).

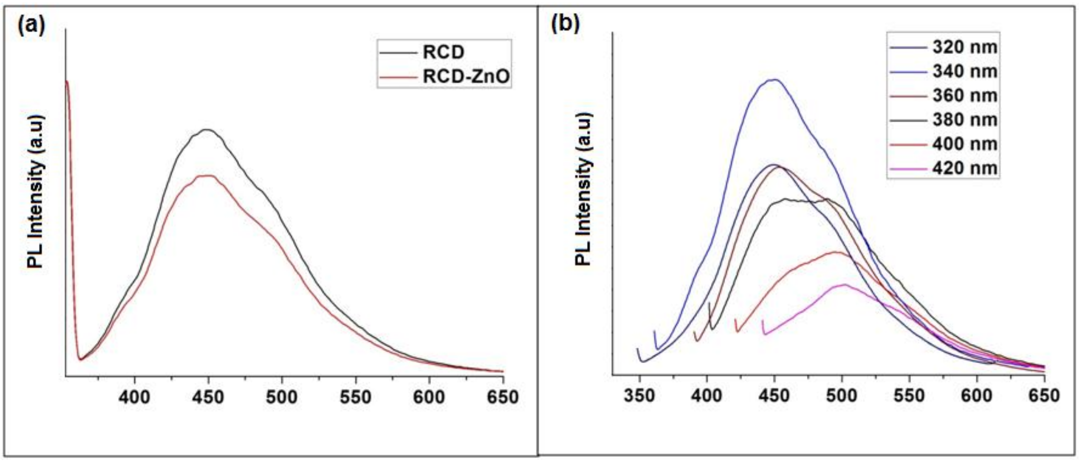

Figure 5.13. (a) PL spectra of RCD and RCD-ZnO (1 mg mL^{-1}) at 340 nm excitation and **(b)** PL spectra of RCD-ZnO with variation of excitation wavelength (320-420) nm.

It was observed that the PL intensity of RCD-ZnO was considerably reduced compared to that of RCD. This reduction in PL intensity suggested delay in recombination of photo-generated charge carriers in the RCD-ZnO heterostructure, resulting from the effective charge transfer between ZnO phase and RCD phase of the nanohybrid [29]. Therefore, RCD-ZnO has better photocatalytic efficiency than RCD and hence it is used as a nano-reinforcing agent in fabrication of HPU/RZN nanocomposites. Furthermore, the RCD-ZnO nanohybrid also displayed excitation wavelength-dependent PL emission in the excitation wavelength range of 320-420 nm, reaching florescence maximum at an excitation of 340 nm (**Figure 5.13b**).

5.3.8. Photocatalytic activity

A prospective mechanism (**Scheme 5.3**) of photocatalytic degradation of surfactants using solar light was proposed. Photocatalysis based on nanoparticle involves effective capturing of solar light, generation of e^-/h^+ pairs and efficient use of e^-, h^+, or both prior to their recombination. Nevertheless, for a semiconductor nanoparticle, the excitation recombination lifetime is usually on the picoseconds scale [30].

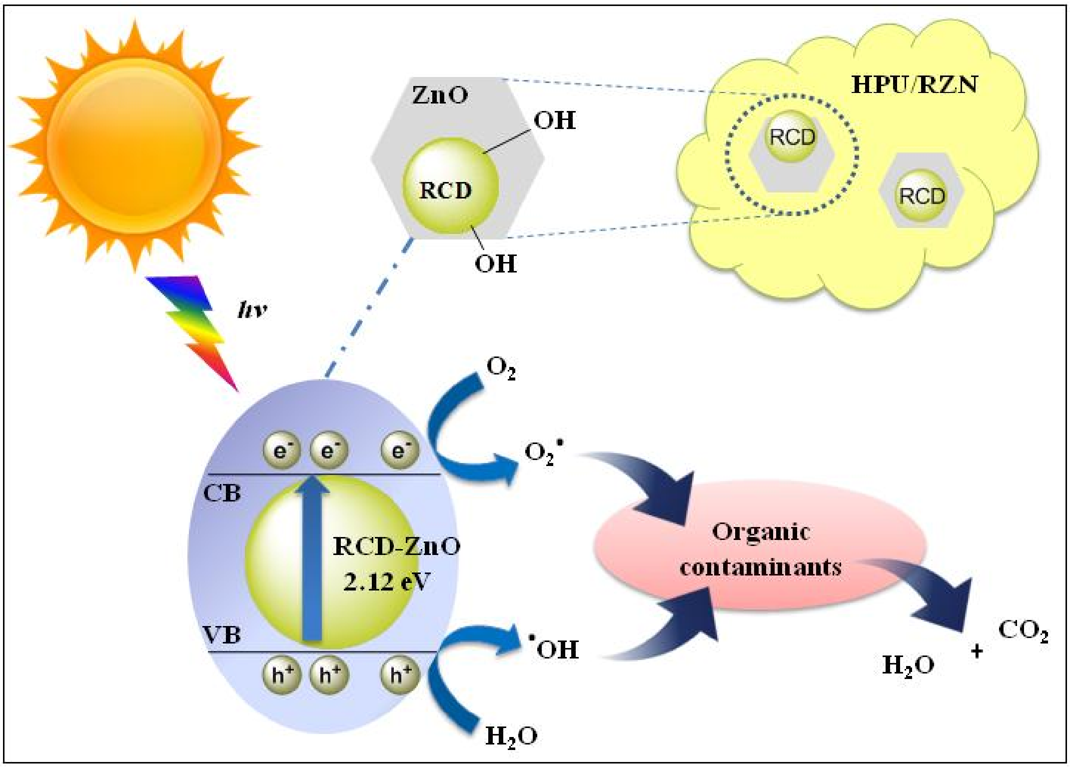

Scheme 5.3. Photocatalytic degradation mechanism by HPU nanocomposite.

As a result, quick excitation recombination leads to ineffective photocatalytic reactions. Herein, RCD-ZnO nanohybrid was mainly selected for two reasons. First reason being, RCD-ZnO was used to capture solar light with reduction in the effective band gap of RCD and ZnO. And second, RCD-ZnO can delay the e^-/h^+ pair recombination of RCD which allows efficient charge separation and photocatalytic activity. The strong electrostatic interaction between anionic RCD and cationic ZnO enhances the above factors. The electrostatic force among ZnO and RCD results in tunneling of photo-excited e^-s which is employed for photocatalytic degradation of surfactants. Furthermore, the high surface area and polar peripheral functional groups of the nanohybrid makes it accessible to the surfactants. Thus, the nanohybrid was found to be a suitable photocatalyst for the efficient degradation of surfactants and detergents. The surface plasmon of ZnO is excited by solar light which results in the coherent oscillation of e^-, thus producing a high concentration of energetic e^- on their surface. The π-conjugated RCD surface adjacent to ZnO rapidly transports the e^- by its extended π-conjugation and efficiently separates the e^-/h^+ pairs. Basically, the low band gap of nanohybrid results in this phenomenon of e- transfer. The e^- react with dissolved O_2 to generate reactive oxidative species ($^{\bullet}O^{2-}$, O_2^{2-}) whereas the h^+ on ZnO might react with H_2O molecules to generate $^{\bullet}OH$ radicals. The degradation of the OC is caused by these reactive oxidative species by an oxidative pathway. The literature cites the photocatalytic degradation of organic molecules into smaller molecules with a few intermediates [31]. Giahi *et al.* reported the complete degradation of 30 mg L^{-1} linear alkyl benzene in presence of 0.2 g L^{-1} ZnO under UV irradiation for 0 to 2 h [5]. Again, Samadi *et al.* degraded 98% of 10 mg L^{-1} anionic surfactant using 150 mg L^{-1} ZnO nano powder under UV irradiation for 40 min [6]. Again, Szabo-Bardos *et al.* reported complete photocatalytic degradation of 300 mg L^{-1} of lauryl benzenesulfonate using 1 g dm^{-3} TiO_2 under UV irradiation for 6 h [32].

In the current study, it was observed that 0.5 g of HPU/RZN2 nanocomposite film can degrade 96% of DBS and 94% of detergent in water under 110 min and 150 min of solar light irradiation, respectively. The photocatalytic degradation of surfactants and detergents is shown by the plots of optical absorbance against wavelength for both HPU/RZN and RCD-ZnO at different times (**Figure 5.14a** and **b**). The effective degradation of the surfactants is exhibited by their concentration changes with time as determined by UV absorbance (**Figure 5.15a** and **b**). Moreover, to determine the effect of superiority of HPU/RZN2 nanocomposite in comparison to RCD-ZnO nanohybrid, the photocatalytic degradation of the surfactant and detergent was conducted using the nanohybrid.

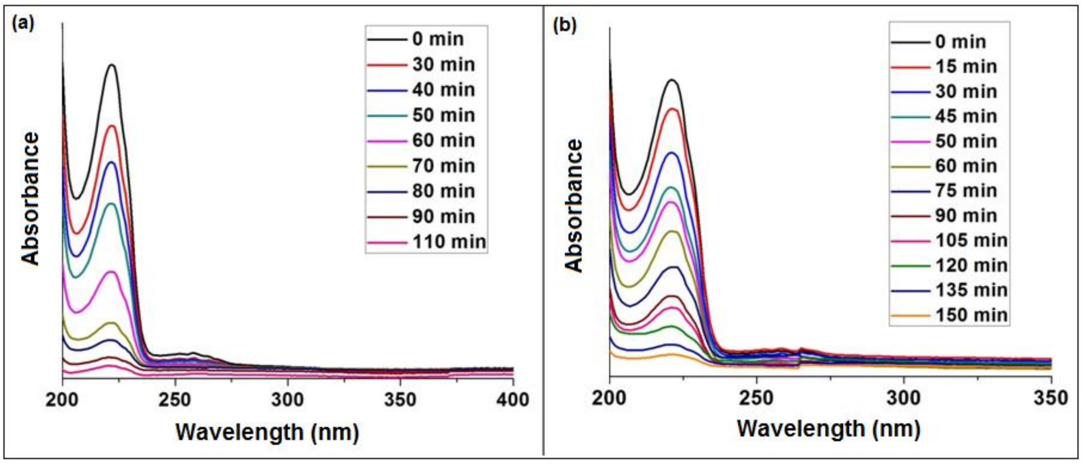

Figure 5.14. Plots of UV absorbance against wavelength at different times for the degradation of **(a)** DBS and **(b)** commercial detergent in the presence of sunlight.

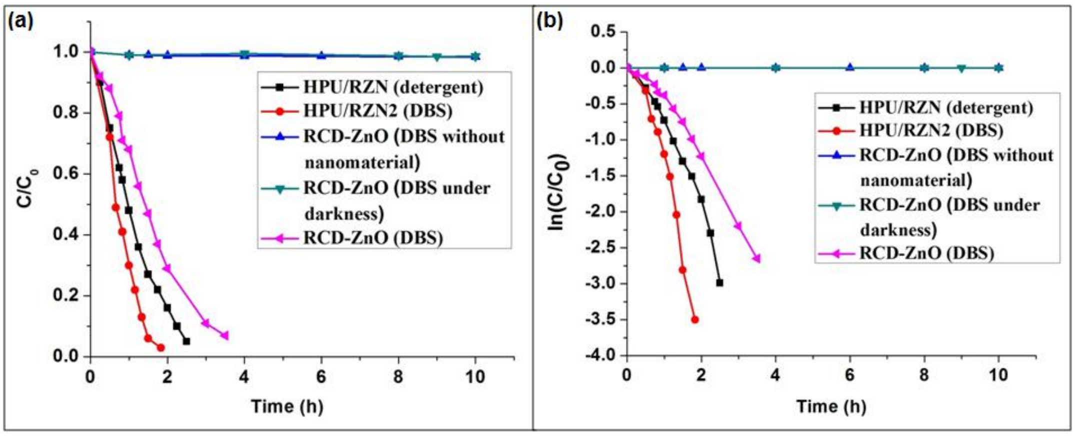

Figure 5.15. (a) Degradation curves and **(b)** fitting degradation curves of DBS and detergent under given conditions.

It was observed that 0.01 g of RCD-ZnO required 3.5 h of sunlight irradiation for 95% degradation of DBS. The superiority of the HPU nanocomposite over the nanohybrid is evidently indicated by the results. The polar functional groups of HPU may interact with that of the organic pollutants and adhere on the surface, facilitating strong interaction with active oxygen radicals. Therefore, the nanocomposite has improved catalytic effectiveness owing to its good interaction with the nanohybrid and its ability to avoid leaching of the materials. The photocatalytic degradation is also performed under dark condition with the nanohybrid. The results indicated that even after 10 h, there was no decrease of intensity as measured by UV-visible spectroscopy. Therefore, the possibility of elimination of the organic pollutants by adsorption of the nanomaterials is eliminated. To demonstrate the self-degradation of the OC, additional experiments were designed without use of nanomaterials under sunlight. The results indicated that 10 h of solar irradiation displayed no decrease in their intensities which ruled out the possibility of self-degradation of the OC (**Figure 5.15a and b**). To illustrate the photodegradation performance of the HPU nanocomposites, the pseudo-first order kinetic model equation is used.

$-dC/dt = K_1t$………………………………………. **(Eq. 5.4)**

Where K_1 = apparent rate constant, C = concentration of pollutants and t = time. On integration of equation (ii), the following equation is obtained:

$\ln(C/C_0) = -K_1t$……………………………………..**(Eq. 5.5)**

Where C_0 = initial concentration (at t = 0) of the OC. The fitting plots of $\ln(C/C_0)$ versus time display the photocatalytic degradation of surfactants with over 0.94 fitting coefficients, which represents a regular photo-degradation behavior. However, the nano-level dispersion of nanohybrid catalyst in water makes its recovery difficult. This results in the requirement of a large quantity of solvent and high speed centrifugation 7000-10,000 rpm for the recovery of the nanohybrid catalyst. Alternatively, the nanocomposite film can be effortlessly recovered from the reaction medium and therefore, can be efficiently recycled. The catalyst was investigated for its recyclability under sunlight for DBS degradation. It was observed that there was no reduction in photocatalytic efficiency even after five repeated recycling of the nanocomposite (**Figure 5.16**). For a heterogeneous recyclable photocatalyst, the mechanical integrity must be retained. Such photocatalysts should have adequate mechanical properties so that they can be recycled repeatedly, without losing their mechanical strength and thereby prevent the leaching of the nanohybrid from the matrix. In this case, HPU/RZN2 is mechanically robust, hence it can be recycled up to five cycles. To further improve the surface area, the nanocomposite film was chopped into very small pieces and dispersed into the OC solution for effective access of its surface. The products formed at the end of the photocatalytic degradation of the surfactants are assumed to be CO_2 and H_2O.

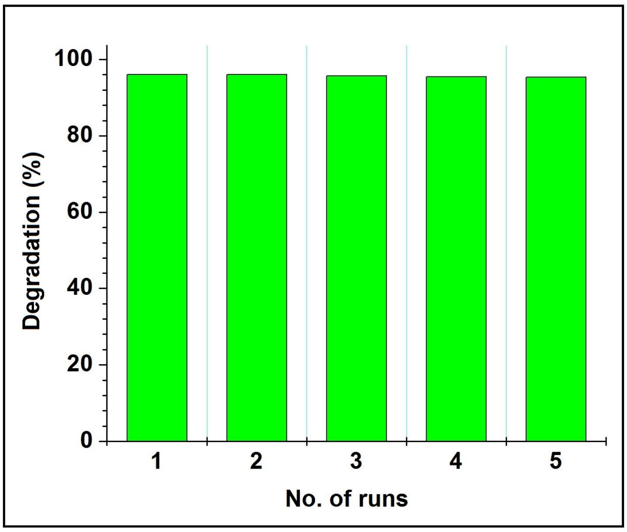

Figure 5.16. Photocatalytic degradation of DBS using recycled HPU/RZN2 five successive times.

5.4. Conclusion

A facile one-pot technique was employed to synthesize reduced carbon dot-zinc oxide nanohybrid (RCD-ZnO) which primarily resulted in the reduction of optical band gap. The fabrication of starch modified hyperbranched polyurethane nanocomposite (HPU/RZN) with as-synthesized RCD-ZnO nanohybrid by *in situ* polymerization technique demonstrated solar assisted photocatalytic degradation of a surfactant and a commercial detergent in aqueous medium. Moreover, the mechanical and thermal properties of the nanocomposites can be tailored by suitable preference of nanohybrid loading and fabrication process. The nanocomposite verified remarkable effectiveness for the photocatalytic degradation of the surfactant and detergent under sunlight. Therefore, the fabricated nanocomposite can provide environmental remediation as a prospective solar light assisted recyclable photocatalyst for water decontamination.

References

[1] Dutta, S. K., Mehetor, S. K., and Pradhan, N. Metal semiconductor heterostructures for photocatalytic conversion of light energy. *The Journal of Physical Chemistry Letters*, 6(6):936-944, 2015.

[2] Ye, L., Su, Y., Jin, X., Xie, H., and Zhang, C. Recent advances in BiOX (X= Cl, Br and I) photocatalysts: synthesis, modification, facet effects and mechanisms. *Environmental Science: Nano*, 1(2):90-112, 2014.

[3] Reddy, K. R., Karthik, K. V., Benaka Prasad, S. B., Soni, S. K., Jeong, H. M., and Raghu, A. V. Enhanced photocatalytic activity of nanostructured titanium dioxide/polyaniline hybrid photocatalysts. *Polyhedron*, 120:169-174, 2016.

[4] Ansari, S. A. and Cho, M. H. Highly visible light responsive, narrow band gap TiO_2 nanoparticles modified by elemental red phosphorus for photocatalysis and photoelectrochemical applications. *Scientific Reports*, 6:25405, 2016.

[5] Giahi, M. and Toutounchi, S. Synthesis of ZnO nanoparticles and its application in photocatalytic degradation of LABS by the trial-and-error and Taguchi methods. *Russian Journal of Applied Chemistry*, 89(13):823-829, 2016.

[6] Samadi, M. T., Dorraji, M. S., Atashi, Z., and Rahmani, A.R. Photo catalytic removal of sodium dodecyl sulfate from aquatic solutions with prepared ZnO

nanocrystals and UV irradiation. *Avicenna Journal of Environmental Health Engineering*, 1(1):166, 2014.

[7] Xu, J., Cui, Y., Han, Y., Hao, M., and Zhang, X. ZnO-graphene composites with high photocatalytic activities under visible light. *RSC Advances*, 6(99):96778-96784, 2016.

[8] Zhang, J., Jin, X., Morales-Guzman, P. I., Yu, X., Liu, H., Zhang, H., Razzari, L., and Claverie, J. P. Engineering the absorption and field enhancement properties of Au-TiO_2 nanohybrids via whispering gallery mode resonances for photocatalytic water splitting. *ACS Nano*, 10(4):4496-4503, 2016.

[9] Zhang, N., Zhang, Y., and Xu, Y. J. Recent progress on graphene-based photocatalysts: current status and future perspectives. *Nanoscale*, 4(19):5792-5813, 2012.

[10] Sun, Y., Wu, Q., and Shi, G. Graphene based new energy materials. *Energy & Environmental Science*, 4(4):1113-1132, 2011.

[11] Thakur, S. and Karak, N. Alternative methods and nature-based reagents for the reduction of graphene oxide: a review. *Carbon*, 94 224-242, 2015.

[12] Thakur, S. and Karak, N. Green reduction of graphene oxide by aqueous phytoextracts. *Carbon*, 50(14):5331-5339, 2012.

[13] Thakur, S. and Karak, N. Tuning of sunlight-induced self-cleaning and self-healing attributes of an elastomeric nanocomposite by judicious compositional variation of the TiO_2-reduced graphene oxide nanohybrid. *Journal of Materials Chemistry A*, 3(23):12334-12342, 2015.

[14] Pasquet, J., Chevalier, Y., Pelletier, J., Couval, E., Bouvier, D., and Bolzinger, M. The contribution of zinc ions to the antimicrobial activity of zinc oxide. *Colloids and Surfaces A: Physicochemical and Engineering*, 457(1):263-274, 2014.

[15] Zhang, X., Zhang, Y., and Ma, L. One-pot facile fabrication of graphene-zinc oxide composite and its enhanced sensitivity for simultaneous electrochemical detection of ascorbic acid, dopamine and uric acid. *Sensors & Actuators, B: Chemical*, 227:488-496, 2016.

[16] Saranya, M., Ramachandran, R., and Wang, F. Graphene-zinc oxide (G-ZnO) nanocomposite for electrochemical supercapacitor applications. *Journal of Science: Advanced Materials and Devices*, 1(4):454-460, 2016.

[17] Hana, C., Li, Z., and Shen, J., Photocatalytic degradation of dodecyl-benzenesulfonate over TiO_2-Cu_2O under visible irradiation. *Journal of Hazardous Materials*, 168(1):215-219, 2009.

[18] Jardak, K., Drogui, P., and Daghrir, R. Surfactants in aquatic and terrestrial environment: occurrence, behavior, and treatment processes. *Environmental Science and Pollution Research*, 23(4):3195, 2016.

[19] Bautista-Toledo, M. I., Rivera-Utrilla, J., Mendez-Díaz, J. D., Sanchez-Polo, M., and Carrasco-Marín, F. Removal of the surfactant sodium dodecylbenzenesulfonate from water by processes based on adsorption/bioadsorption and biodegradation. *Journal of Colloid and Interface Science*, 418:113-119, 2014.

[20] Gogoi, S., Kumar, M., Mandal, B. B., and Karak, N. High performance luminescent thermosetting waterborne hyperbranched polyurethane/carbon quantum dot nanocomposite with in vitro cytocompatibility. *Composites Science and Technology*, 118:39-46, 2015.

[21] De, B. and Karak, N. A green and facile approach for the synthesis of water soluble fluorescent carbon dots from banana juice. *RSC Advances*, 3(22):8286-8290, 2013.

[22] Bala, N., Saha, S., Chakraborty, M., Maiti, M., Das, S., Basu, R., and Nandy, P. Green synthesis of zinc oxide nanoparticles using Hibiscus subdariffa leaf extract: effect of temperature on synthesis, anti-bacterial activity and anti-diabetic activity. *RSC Advances*, 5(7):4993-5003, 2015.

[23] Abdullah, K. A., Awad, S., Zaraket, J., and Salame, C. Synthesis of ZnO nanopowders by using sol-gel and studying their structural and electrical properties at different temperature. *Energy Procedia*, 119:565-570, 2017.

[24] Guangyao, X., Honglin, L., Jing, Z., Jun, J., and Yizao, W. Synthesis of ZnO by chemical bath deposition in the presence of bacterial cellulose. *Acta Metallurgica Sinica*, 27(4):656-662, 2014.

[25] Das, B., Mandal, M., Upadhyay, A., Chattopadhyay, P., and Karak, N. Bio-based hyperbranched polyurethane/Fe_3O_4 nanocomposites: smart antibacterial biomaterials for biomedical devices and implants. *Biomedical Materials*, 8(3):035003, 2013.

[26] Thakur, S. and N. Karak, Multi-stimuli responsive smart elastomeric hyperbranched polyurethane/reduced graphene oxide nanocomposites. *Journal of Materials Chemistry*, 2(36):14867-14875, 2014.

[27] Talam, S., Karumuri, S. R., and Gunnam, N. Synthesis, characterization, and spectroscopic properties of ZnO nanoparticles. *ISRN Nanotechnology*, 2012:1-6, 2012.

[28] Yousefi, R., Jamali-Sheini, F., Cheraghizade, M., Khosravi-Gandomani, S., Sáaedi, A., Huang, N. M., Basirun, W. J., and Azarang, M. Enhanced visible-light photocatalytic activity of strontium-doped zinc oxide nanoparticles. *Materials Science in Semiconductor Processing*, 32:152-159, 2015.

[29] Li, Y. Zhang, B. P., Zhao, J. X., Ge, Z. H., Zhao, X. K., and Zou, L. ZnO/carbon quantum dots heterostructure with enhanced photocatalytic properties. *Applied Surface Science*, 279:367-373, 2013.

[30] Kaniyankandy, S., Rawalekar, S., and Ghosh, H. N. Ultrafast charge transfer dynamics in photoexcited CdTe quantum dot decorated on graphene. *Journal of Physical Chemistry C*, 116(30):16271-16275, 2012.

[31] Bhunia, S. K. and Jana, N. R. Reduced graphene oxide-silver nanoparticle composite as visible light photocatalyst for degradation of colorless endocrine disruptors. *ACS Applied Materials & Interfaces*, 6(22):20085-20092, 2014.

[32] Szabo-Bardos, E., Zsilak, Z., and Horvath, O. Photocatalytic Degradation of Anionic Surfactant in Titanium Dioxide Suspension, In *Colloids for Nano-and Biotechnology*, pages 21-28, ISBN: 978-3-540-85133-2. Springer, 2008.